Quantum Geometry and the Electric Magnetochiral Anisotropy in Noncentrosymmetric Polar Media

Pierpaolo Fontana,[1] Victor Velasco,[2] Chang Niu,[3,4] Peide D. Ye,[3,4] Pedro V. Lopes,[5] Kaio E. M. de Souza,[6] Marcus V. O. Moutinho,[6] Caio Lewenkopf,[5] and Marcello B. Silva Neto[5]

[1]*Departament de Física, Universitat Autònoma de Barcelona, 08193 Bellaterra, Spain*
[2]*International School for Advanced Studies (SISSA), Via Bonomea 265, I-34136 Trieste, Italy*
[3]*Elmore Family School of Electrical and Computer Engineering, Purdue University, West Lafayette, Indiana 47907, USA*
[4]*Birck Nanotechnology Center, Purdue University, West Lafayette, Indiana 47907, USA*
[5]*Instituto de Física, Universidade Federal do Rio de Janeiro, 21941-972 Rio de Janeiro, Brazil*
[6]*Universidade Federal do Rio de Janeiro–Campus UFRJ Duque de Caxias, 25240-005, Duque de Caxias, Rio de Janeiro, Brazil*

(Received 24 February 2025; revised 6 June 2025; accepted 11 August 2025; published 2 September 2025)

The electric magnetochiral anisotropy is a nonreciprocal phenomenon accessible via second harmonic transport in noncentrosymmetric, time-reversal invariant materials, in which the rectification of current, $\mathbf{I}$, can be controlled by an external magnetic field, $\mathbf{B}$. Quantum geometry, which characterizes the topology of Bloch electrons in a Hilbert space, provides a powerful description of the nonlinear dynamics in topological materials. Here, we demonstrate that the electric magnetochiral anisotropy in noncentrosymmetric polar media owes its existence to the quantum metric, arising from the spin-orbit coupling, and to large Born effective charges. In this context, the reciprocal magnetoresistance $\beta\mathbf{B}^2$ is modified to $R(I,P,B) = R_0[1+\beta B^2+\gamma^{\pm}\mathbf{I}\cdot(\mathbf{P}\times\mathbf{B})]$, where the chirality dependent $\gamma^{\pm}$ is determined by the quantum metric dipole and $\mathbf{P}$ is the polarization. In 2D, we predict a universal scaling $\gamma^{\pm}(V)\sim V^{-5/2}$, which we compare to available phase sensitive, second harmonic transport measurements on hydrothermally grown tellurium films under applied gate voltage, V. The control of rectification by varying $\mathbf{I}$, $\mathbf{P}$, $\mathbf{B}$, and V, demonstrated in this work, opens up new avenues for the building of ultrascaled complementary metal-oxide-semiconductor circuits.

DOI: 10.1103/7nxc-j62y

Introduction—Nonreciprocal transport phenomena occur when the flow of charge, such as electrons and holes in semiconductors, depends on the direction of the current, resulting in an asymmetric conduction. In pn junctions, this nonreciprocity arises from the interface between p-type and n-type semiconductor materials, where a built-in electric field creates a depletion region that allows current to flow more easily in one direction than in the other [1]. This behavior is fundamental to the operation of diodes, acting as one-way gates for current flow and enabling rectification of alternating currents, signal modulation, and voltage regulation [2].

One of the basic ingredients of nonreciprocal phenomena is the lack of inversion symmetry in chiral molecules, films, or crystals [3]. Noncentrosymmetry leads to directional propagation of quantum particles, giving rise to various phenomena such as the natural optical activity in chiral materials [4]; the nonreciprocal magnon transport or spin current in chiral magnets [5]; the conversion of a coherent lattice vibration into a quasistatic structural distortion in nonlinear phononics [6]; and the unidirectional magnetoresistance, or electrical magnetochiral anisotropy (eMChA), in polar and chiral semiconductors [7]. The eMChA is a nonreciprocal phenomenon observed in materials with a large magnetoresistance, such as a Si-based field effect transistor [8]. Other systems also exhibit this type of unidirectional magnetoresistance, such as the polar semiconductor BiTeBr [9]; the multiferroic semiconductor (Ge, Mn)Te [10]; and nonpolar systems, such as the topological insulator nanowire heterostructure $(Bi_{1-x}Sb_2)_2Te_3$ under applied voltage bias [11], twisted bilayer graphene [12], and the topological semimetal $ZrTe_5$ [13]. In all of these systems, the ability to control rectification using external parameters such as current, voltage, polarization, and magnetic field opens up new possibilities for the design of, for instance, ultrascaled complementary metal-oxide-semiconductor circuits [14].

The underlying mechanism responsible for the nonreciprocal carrier diffusion in polar media can be elegantly understood through a heuristic argument proposed by Rikken [8]. This mechanism is the transport analog of an optical phenomenon observed when light with wave vector $\mathbf{k}$ propagates perpendicularly to crossed electric $\mathbf{E}$ and magnetic $\mathbf{B}$ fields [15]. In this context, the effective refractive index receives a relativistic contribution of the form $\delta n\sim\mathbf{k}\cdot\mathbf{v}$, obtained by means of a Lorentz transformation

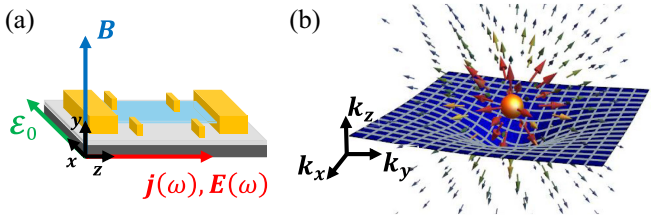

FIG. 1. (a) Setup used in this work. The static and uniform electric, $\boldsymbol{\mathcal{E}}_0 \| x$, and magnetic, $\mathbf{B} \| y$, fields are perpendicular to the flow of the ac-current $\mathbf{j}(\omega) \| z$ and voltage related, ac-electric field $\mathbf{E}(\omega) \| z$. (b) Topological singularities, such as a Weyl node, introduce both a radial spin texture (and Berry curvature) and momentum space geodesics (white grid) for the adiabatic evolution of quantum states.

to a moving frame with velocity $\mathbf{v} = c\mathbf{E} \times \mathbf{B}/B^2$ with respect to the laboratory [16]. Rikken argued that an analogous mechanism applies to diffusive transport [8]. When a current $\mathbf{I} \sim \langle \mathbf{k} \rangle$ flows perpendicularly to crossed electric ($\boldsymbol{\mathcal{E}}_0$) and magnetic ($\mathbf{B}$) fields, see Fig. 1(a), the reciprocal magnetoresistance, $\Delta R/R = 1 + \beta \mathbf{B}^2$, acquires a nonreciprocal, relativistic correction of the form $\delta R/R = 2\gamma \mathbf{I} \cdot (\boldsymbol{\mathcal{E}}_0 \times \mathbf{B})$. This correction arises because, in the laboratory frame, the motion of a charged particle acquires an *additional drift velocity* $\mathbf{v} = c\boldsymbol{\mathcal{E}}_0 \times \mathbf{B}/B^2$. The field $\boldsymbol{\mathcal{E}}_0$ can represent an applied electric field, the field due to a net polarization $\mathbf{P}$ in noncentrosymmetric materials, or the field resulting from a band offset at the interface of semiconductor heterostructures [8]. Rikken further conjectured that the nonlinear conductivity would be given by $\tilde{\sigma}_{ij}(\langle \mathbf{k} \rangle \cdot \boldsymbol{\mathcal{E}}_0 \times \mathbf{B})$ [8], extending Onsager's reciprocity relations for time-reversal invariant systems [17], and it would be accessible via second harmonic transport experiments.

In this Letter, we demonstrate that Rikken's conjecture arises naturally from the quantum geometric properties [18] of noncentrosymmetric media, which are characterized by strong spin-orbit interactions (relativistic corrections) and large Born effective charges (macroscopic polarization). Using Boltzmann's semiclassical approach [19], we show how the quantum metric dipole (QMD) constrains the geodesic flow of velocities in Hilbert space [20–23], generating a nonzero component for the longitudinal current from the Lorentz force and a nonlinear magnetoconductivity of the form $\tilde{\sigma}_{ij}(\langle \mathbf{v} \rangle_{\mathrm{QMD}} \cdot \boldsymbol{\mathcal{E}}_0 \times \mathbf{B})$. To validate our results we performed density functional theory (DFT) calculations to estimate the polar electric field, $\boldsymbol{\mathcal{E}}_0$, and compared our findings to phase-sensitive, second harmonic transport measurements in 2D n-type tellurium films at low temperature, varying both the applied magnetic field and the gate voltage [24]. We show, unambiguously, that the eMChA in 2D tellurium is polar, not chiral, deviating from the chiral eMChA recently demonstrated for chiral conductors [25]. This finding is significant for a material relevant for materials science and electronics [26].

Second harmonics—The polarization-induced eMChA is a nonlinear phenomenon described by the relation

$$R(I, B, P) = R_0[1 + \beta B^2 + \gamma^{\pm} \mathbf{I} \cdot (\mathbf{P} \times \mathbf{B})], \tag{1}$$

where R_0 is the resistance, β is the reciprocal magnetoresistance coefficient, and $\gamma^{\pm}$ is the nonreciprocal eMChA coefficient for the two possible chiralities [8,15,27]. This phenomenon is described by a fourth-rank tensor, $\mathbf{G}$, in the expansion of the ac current density, $\mathbf{j}$, in powers of the ac electric field strength and the magnetic field [28]:

$$j_i = \sigma_{ij} E_j + \sigma_{ijk}^{(H)} E_j B_k + G_{ijk\ell} E_j E_k B_\ell. \tag{2}$$

Here, σ_{ij} is the linear conductivity, and $\sigma_{ijk}^{(H)}$ represents the Hall conductivity. The eMChA is encoded in the tensor $\mathbf{G}$, symmetric in j and k. By solving for $\mathbf{E}$ as a function of $\mathbf{B}$ and $\mathbf{j}$ up to order Bj^2, the tensor $\mathbf{G}$ is [28]

$$G_{ijk\ell} \propto \gamma_{ij'k'\ell} \sigma_{j'j} \sigma_{k'k}, \tag{3}$$

and the fourth-rank tensor $\gamma_{ijk\ell}$ characterizes the second-harmonic generation described by $E_i^{2\omega} = \gamma_{ijkl} j_j^{\omega} j_k^{\omega} B_l$, under conditions of a long period $T = 2\pi/\omega$ [27,28]. The relative nonreciprocal resistance therefore reads as [29]

$$\frac{4V_{zz}^{2\omega}}{V_{zz}^{\omega}} = \frac{\Delta R}{R_0} = 2\gamma^{\pm} \mathbf{I} \cdot (\mathbf{P} \times \mathbf{B}), \tag{4}$$

and the eMChA coefficient, $\gamma^{\pm}$, introduced in Eq. (1) for an isotropic system, scales as $\gamma^{\pm} \sim G/\sigma$.

Quantum geometry—The existence of a nonlinear conductivity, even at the smallest perturbation, has been recently claimed to have a quantum geometric origin [18]. Quantum mechanics can be formulated as a geometric theory in a Hilbert space, where the distance between adjacent quantum states $|n_{\mathbf{k}}\rangle$ and $|n_{\mathbf{k}+d\mathbf{k}}\rangle$ in the nth band is determined by the *quantum geometric tensor* [31],

$$\mathcal{Q}^n(\mathbf{k}) = \mathbf{g}^n(\mathbf{k}) - \frac{i}{2} \boldsymbol{\Omega}^n(\mathbf{k}). \tag{5}$$

The Berry curvature, $\boldsymbol{\Omega}^n(\mathbf{k})$, has long been recognized to generate several important linear transport phenomena, such as the quantum anomalous Hall effect [32,33], due to its role as a magnetic field in reciprocal space. In contrast, the quantum metric tensor, $\mathbf{g}^n(\mathbf{k})$, has only recently been experimentally probed, through nonlinear transport measurements, such as the nonlinear Hall effect and nonlinear magnetoresistance [21], and angle-resolved photoemission spectroscopy [34]. The quantum metric constrains Bloch electrons to follow momentum space geodesics [23], as shown in Fig. 1(b), thereby modifying the wave packet dynamics. The calculation of $\mathbf{g}^n(\mathbf{k})$ and $\boldsymbol{\Omega}^n(\mathbf{k})$ is

straightforward for a 2×2 Hamiltonian $\mathcal{H}=\mathbf{d}(\mathbf{k})\cdot\boldsymbol{\sigma}$, where $\boldsymbol{\sigma}=(\sigma_x,\sigma_y,\sigma_z)$ are Pauli matrices and $\mathbf{d}$ is a 3D-vector. In this case, for the two bands $n=\pm$ and with $\partial_a\equiv\partial/\partial k_a$, we have

$$\mathbf{g}^{\pm}_{ab}=\frac{1}{4d^2}\left[\partial_a\mathbf{d}\cdot\partial_b\mathbf{d}-\frac{1}{d^2}(\partial_a\mathbf{d}\cdot\mathbf{d})(\partial_b\mathbf{d}\cdot\mathbf{d})\right],$$
$$\boldsymbol{\Omega}^{\pm}_{ab}=\mp\frac{(\partial_a\mathbf{d}\times\partial_b\mathbf{d})\cdot\mathbf{d}}{2d^3}. \tag{6}$$

Boltzmann transport—We compute the current density (V is the volume of the unit cell),

$$\mathbf{j}=-\frac{e}{V}\sum_{n,\mathbf{k}}\dot{\mathbf{r}}_n f_n(\mathbf{k}), \tag{7}$$

up to order E^2B in Eq. (2). Here, $f_n(\mathbf{k})$ is the non-equilibrium distribution, satisfying the Boltzmann transport equation in the relaxation time approximation [19]

$$\frac{\partial f_n(\mathbf{k})}{\partial t}+\dot{\mathbf{r}}_n\cdot\frac{\partial f_n(\mathbf{k})}{\partial\mathbf{r}}+\dot{\mathbf{k}}_n\cdot\frac{\partial f_n(\mathbf{k})}{\partial\mathbf{k}}=-\frac{\delta f_n(\mathbf{k})}{\tau_{\mathbf{k}}}, \tag{8}$$

and $\delta f_n(\mathbf{k})=f_n(\mathbf{k})-f^0_n(\mathbf{k})$, where $f^0_n(\mathbf{k})=1/(e^{\beta[\varepsilon_n(\mathbf{k})-\mu]}+1)$ is the equilibrium Fermi-Dirac distribution, $\varepsilon_n(\mathbf{k})$ is the dispersion relation of the n band, $\beta=1/k_BT$ is the inverse temperature, μ is the chemical potential, and $\tau_{\mathbf{k}}$ is the relaxation time near a high-symmetry point in the Brillouin zone due to elastic scattering from impurities [35–37]. For homogeneous systems $\partial f_n/\partial\mathbf{r}=0$. The velocity, $\dot{\mathbf{r}}_n$, and the acceleration, $\dot{\mathbf{k}}_n$, are defined by the semiclassical equations of motion [23]:

$$\dot{\mathbf{r}}_n=\mathbf{v}^n_{\mathbf{k}}+\dot{\mathbf{k}}_n\times\boldsymbol{\Omega}^n_{\mathbf{k}}+\dot{\mathbf{k}}_n\cdot\hbar\boldsymbol{\Gamma}^n(\partial\mathbf{g})\cdot\dot{\mathbf{k}}_n, \tag{9}$$

$$\hbar\dot{\mathbf{k}}_n=-e(\mathbf{E}+\boldsymbol{\mathcal{E}}_0)-e\dot{\mathbf{r}}_n\times\mathbf{B}, \tag{10}$$

where $\boldsymbol{\mathcal{E}}_0$ is a static and uniform electric field resulting from the macroscopic polarization and we assumed $c=1$. In Eq. (9), the first term, $\mathbf{v}^n_{\mathbf{k}}=(1/\hbar)\nabla_{\mathbf{k}}\varepsilon_n(\mathbf{k})$, represents the bare band velocity; the second term, $\dot{\mathbf{k}}_n\times\boldsymbol{\Omega}^n_{\mathbf{k}}$, is the anomalous velocity, arising from the Berry curvature; and the third term is the geodesic contribution due to the QMD, with $\dot{\mathbf{k}}_n\cdot\boldsymbol{\Gamma}^n(\partial\mathbf{g})\cdot\dot{\mathbf{k}}_n\equiv\boldsymbol{\Gamma}^n_{ij\ell}\dot{\mathbf{k}}_{n,j}\dot{\mathbf{k}}_{n,\ell}$, and the Christoffel symbols, $\boldsymbol{\Gamma}^{\pm}_{ij\ell}=2\partial_i\tilde{\mathbf{g}}^{\pm}_{j\ell}-(\partial_j\tilde{\mathbf{g}}^{\pm}_{\ell i}+\partial_\ell\tilde{\mathbf{g}}^{\pm}_{ij})/2$, given in terms of the energy normalized quantum metric, $\tilde{\mathbf{g}}^{\pm}_{ij}=\mathbf{g}^{\pm}_{ij}/(\varepsilon_{\pm}-\varepsilon_{\mp})$ [20]. This term encodes the effects of quantum geometry on carrier dynamics, Fig. 1(b), leading to a geometric contribution to nonlinear transport.

In the dc limit and in the presence of a static and uniform magnetic field $\mathbf{B}$, $\delta f_n(\mathbf{k})$ has a semiclassical correction due to the Lorentz force [29], as in Eq. (10):

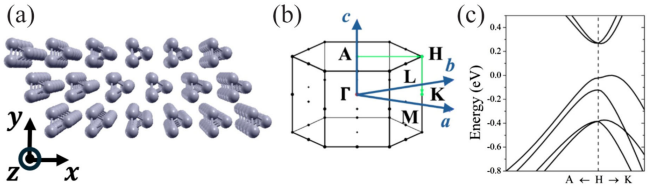

FIG. 2. (a) Trigonal α-Te crystal structure consists of spiral chains with three-fold screw symmetry held together by inter-chain van der Waals bonds. (b) First Brillouin zone of Te. (c) Band features near the direct band edge at the H point along the A-H-K directions.

$$\delta f_n(\mathbf{k})=e\tau_{\mathbf{k}}\left[\dot{\mathbf{r}}_n\cdot\mathbf{E}+e\tau_{\mathbf{k}}\frac{\dot{\mathbf{r}}_n\times\mathbf{B}}{\hbar}\cdot\nabla_{\mathbf{k}}(\dot{\mathbf{r}}_n\cdot\mathbf{E})\right]\left(\frac{\partial f_0}{\partial\varepsilon}\right).$$

Substituting $\dot{\mathbf{r}}_n$ from Eq. (9) into $\delta f_n(\mathbf{k})$ and selecting the contribution from the QMD, $2e^2\mathbf{E}\cdot\boldsymbol{\Gamma}(\partial\mathbf{g})\cdot\boldsymbol{\mathcal{E}}_0/\hbar^2$, the correction to the current at order E^2B becomes

$$\delta\mathbf{j}=\frac{2e^5}{\hbar^2V}\sum_{n,\mathbf{k}}\tau^2_{\mathbf{k}}\mathbf{v}^n_{\mathbf{k}}\{[\mathbf{E}\cdot\boldsymbol{\Gamma}^n(\partial\mathbf{g})\cdot\boldsymbol{\mathcal{E}}_0]\times\mathbf{B}\}\cdot\nabla_{\mathbf{k}}(\mathbf{v}^n_{\mathbf{k}}\cdot\mathbf{E})\left(-\frac{\partial f_0}{\partial\varepsilon_n}\right).$$

This expression is of the form $\langle\mathbf{v}^n_{\mathbf{k}}\rangle_{\mathrm{QMD}}\cdot\boldsymbol{\mathcal{E}}_0\times\mathbf{B}$, validating Rikken's conjecture [8]. The momentum dependent Christoffel symbols, $\boldsymbol{\Gamma}(\mathbf{k})$, emerge as a QMD contribution to the nonlinear conductivity. Writing $\delta\mathbf{j}$ as $\delta j_i=G_{ijk\ell}E_jE_kB_\ell$, we obtain the eMChA tensor as

$$G_{ijk\ell}=\frac{2e^5}{\hbar^2V}\sum_{n,\mathbf{k}}\tau^2_{\mathbf{k}}v^n_{\mathbf{k},i}[\epsilon_{ab\ell}\Gamma^n_{bkm}(\partial\mathbf{g})\mathcal{E}_{0,m}]\partial_a v^n_{\mathbf{k},j}\left(-\frac{\partial f_0}{\partial\varepsilon_n}\right), \tag{11}$$

where the Levi-Civita symbol is defined as $\epsilon_{xyz}=+1$ and, at low temperatures, the equilibrium distribution derivative reduces to $(-\partial f^0_n/\partial\varepsilon_n)=\delta[\varepsilon_n(\mathbf{k})-\mu]$. The $G_{ijk\ell}$ tensor is nonzero because both $\mathbf{v}_{\mathbf{k}}$ and $\boldsymbol{\Gamma}(\mathbf{k})$ are odd under the transformation $\mathbf{k}\to-\mathbf{k}$, and in the presence of a macroscopic polarization, the electric field $\boldsymbol{\mathcal{E}}_0\neq 0$. Most importantly, $G_{ijk\ell}\sim\tau^2$, and since from Eq. (3) $G_{ijk\ell}\sim\gamma_{ijk\ell}\sigma^2$, with $\sigma\sim\tau$, we conclude that the eMChA tensor, $\gamma_{ijk\ell}$, is intrinsic and is determined entirely by the quantum geometric properties of the material.

n-type 2D tellurium—Tellurium (Te) is a narrow-gap Weyl semiconductor composed of one-dimensional chiral chains arranged in a hexagonal lattice. Its α-Te form is shown in Fig. 2(a), and its two-dimensional counterpart has attracted significant scientific and technological interest due to its promising electronic, optoelectronic, and piezoelectric applications [26]. We investigate n-type 2D Te for two primary reasons: (i) n-type Te hosts a Weyl node at the

TABLE I. Conduction band $\mathbf{k}\cdot\mathbf{p}$ parameters in $\mathcal{H}_c$.

A $\times 10^{-15}$ (eV cm^2)	B $\times 10^{-15}$ (eV cm^2)	S $\times 10^{-9}$ (eV cm)	C $\times 10^{-9}$ (eV cm)	F $\times 10^{-15}$ (eV cm^2)	G $\times 10^{-21}$ (eV cm^2)
6.7	4.2	5.8	3.6	1.7	0.2

H point in the Brillouin zone, near the conduction band minimum, see Figs. 2(b) and 2(c), ensuring strong quantum geometric properties, characterized by $\mathbf{\Gamma}_{ijk} \neq 0$, and (ii) 2D Te films exhibit a nonzero net polarization [38] due to the large Born effective charges associated with the lone pairs, resulting in $\boldsymbol{\mathcal{E}}_0 \neq 0$. Furthermore, in few nanometers thick α-Te films, the carrier concentration in the conduction band can be tuned through gating [24], enabling the study of the G-tensor in Eq. (11) as a function of the chemical potential, μ.

The conduction band of Te is well described by the $\mathbf{k}\cdot\mathbf{p}$ perturbation theory, cast by the Hamiltonian [39]

$$\mathcal{H}_c = \begin{bmatrix} Ak_z^2 + Bk_\perp^2 + Sk_z & Ck_- + iGk_-k_z + Fk_+^2 \\ Ck_+ - iGk_+k_z + Fk_-^2 & Ak_z^2 + Bk_\perp^2 - Sk_z \end{bmatrix}, \tag{12}$$

where $k_\pm = k_x \pm ik_y$, $k_\perp = \sqrt{k_x^2 + k_y^2}$. Up to second order in $\mathbf{k}\cdot\mathbf{p}$, the Hamiltonian includes a linear-in-Sk_z term, Sk_z, due to the lack of inversion symmetry, and a parabolic $Ak_z^2 + Bk_\perp^2$ contribution. Combining $\mathbf{k}\cdot\mathbf{p}$ and spin-orbit perturbations yields off-diagonal, linear-in-$k_\pm$ elements $Ck_\pm$, resulting in a principal Weyl node at the H point. A trigonal warping term, $Fk_\pm^2$, generates satellite Weyl nodes away from the H point, and a term $\pm iGk_\mp k_z$ arises from the $\mathbf{k}$-dependent spin-orbit interaction. All parameters of $\mathcal{H}_c$ can be obtained experimentally, for example, through the analysis of magneto-optical transitions [39], with values listed in Table I.

Expanding $\mathcal{H}_c$ in terms of the identity and Pauli matrices as $\mathcal{H}_c = d_0(\mathbf{k})\mathcal{I} + \mathbf{d}(\mathbf{k})\cdot\boldsymbol{\sigma}$ allows us to calculate $\mathbf{\Omega}_\mathbf{k}^n$ and $\mathbf{g}_\mathbf{k}^n$ using Eq. (6). The G_{zzzy} component of the eMChA tensor, Eq. (11), can be evaluated numerically; see Supplemental Material [29]. For clarity and to gain physical insight, we neglect both the trigonal warping, $F = 0$, and the $\mathbf{k}$-dependent spin-orbit interaction, $G = 0$, the smallest parameters in Table I. These simplifications allow us to describe the conduction bands by

$$\varepsilon_\pm(\mathbf{k}) = Ak_z^2 + Bk_\perp^2 \pm \sqrt{S^2k_z^2 + C^2k_\perp^2}. \tag{13}$$

The z component of the velocity, $v_z^\pm(\mathbf{k})$, for these bands and the nonzero components of the Christoffel symbol, $\Gamma_{xzx}(\mathbf{k})$ and $\Gamma_{zzx}(\mathbf{k})$, are

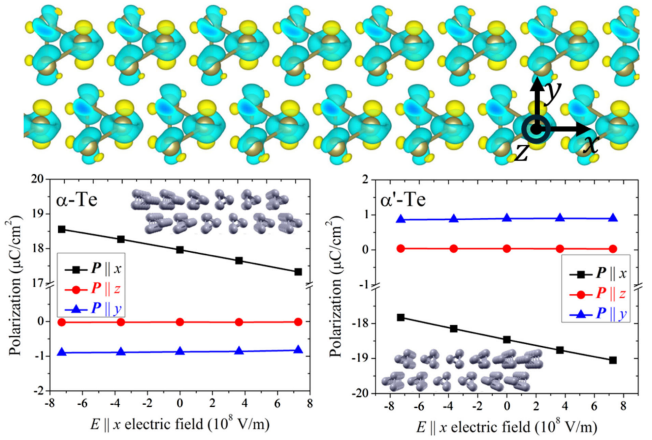

FIG. 3. Lone pairs in 2D α-Te give rise to a net polarization, $\mathbf{P}$, whose largest component is perpendicular to the $\hat{\mathbf{z}}$ (helices) and $\hat{\mathbf{y}}$ (growth) directions, $\mathbf{P}\|\hat{\mathbf{x}}$, and the smallest component $\mathbf{P}\|-\hat{\mathbf{y}}$. The upper panel shows the charge distribution in α-Te, with excess charge represented in yellow and charge deficit given in blue. The macroscopic polarization is also shown in both bottom panels for α and α' Te, as a function of an applied electric field oriented along the x direction.

$$\begin{aligned} v_z^\pm(\mathbf{k}) &= 2Ak_z \pm \frac{k_zS^2}{\sqrt{S^2k_z^2 + C^2k_\perp^2}}, \\ \Gamma_{xzx}^\pm(\mathbf{k}) &= \pm\frac{5S^2C^4k_x^2k_z}{16(C^2k_\perp^2 + S^2k_z^2)^{7/2}}, \\ \Gamma_{zzx}^\pm(\mathbf{k}) &= \frac{k_z}{k_x}\Gamma_{xzx}^\pm(\mathbf{k}). \end{aligned} \tag{14}$$

Away from the Weyl node we can approximate the eigenvalues of $\mathcal{H}_c$ by $\varepsilon_\pm(\mathbf{k}) \approx \hbar^2\mathbf{k}^2/2m_\pm^*$, with $m_+^* < m_-^*$. In this case, the velocity and its k_z derivative are simply given by $\mathbf{v}_\mathbf{k}^\pm = \hbar\mathbf{k}/m_\pm^*$ and $\partial_z v_{\mathbf{k},i}^\pm = \delta_{z,i}\hbar/m_\pm^*$. The normalized eMChA coefficient $\gamma^\pm$ appearing in Eq. (4), $\gamma^\pm(\mu) \equiv G_{zzzy}(\mu)/\sigma(\mu)$, can now be obtained analytically in the constant relaxation time approximation, $\tau_\mathbf{k} = \tau$ [29], with the scaling for $G_{zzzy}(\mu)$ given by [29]

$$G_{zzzy}(\mu) = \frac{G_0}{\mu^{3/2}}, \tag{15}$$

and $G_0 = \hbar e^5\tau^2\boldsymbol{\mathcal{E}}_{0,x}\mathcal{I}[(m_+^*)^{-5/2} - (m_-^*)^{-5/2}]/(2\pi)^2\sqrt{2}$, with the angular integral

$$\mathcal{I}(C,S) = \int_0^{2\pi} d\alpha \frac{5S^2C^4\sin^2(\alpha)\cos^2(\alpha)}{8[C^2\sin^2(\alpha) + S^2\cos^2(\alpha)]^{7/2}}. \tag{16}$$

The final ingredient in Eq. (11), the electric field $\boldsymbol{\mathcal{E}}_0$, arises from the macroscopic polarization in the 2D Te film, $\mathbf{P}$, and should follow the geometry depicted in Fig. 1. DFT calculations [29] for a two-layer Te film, using the Quantum Espresso [40] and Siesta [41] packages, verify

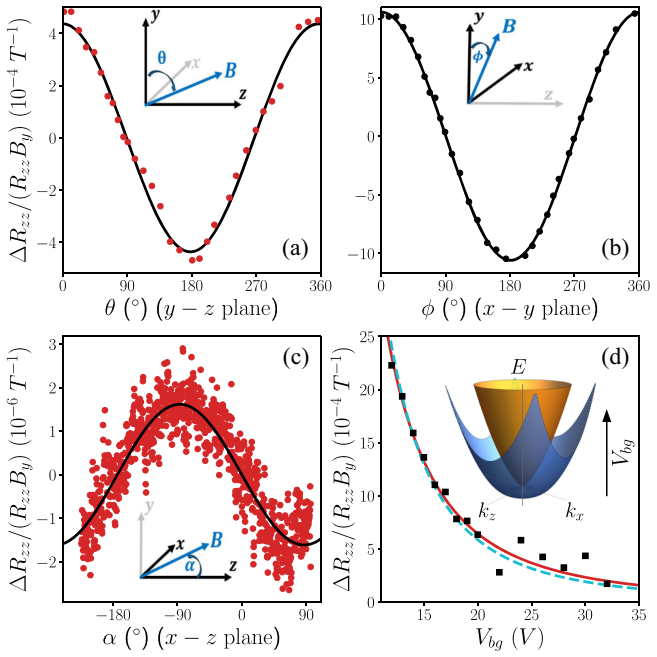

FIG. 4. Electrical magnetochiral anisotropy in 2D Tellurium. (a)–(c) Normalized magnetoresistance $\Delta R_{zz}/(R_{zz}B_y)$ as a function of magnetic field rotation angle in the (a) y-z, (b) x-y, and (c) x-z planes, respectively, demonstrating the predicted polar dependence; see Eq. (4). (d) Backgate voltage dependence of $\Delta R_{zz}/(R_{zz}B_y)$, showing a scaling of $\gamma^{\pm}(V) \sim V^{-5/2}$ (red curve). The dashed blue curve shows the numerical calculated scaling, $\gamma^{\pm}(V) \sim V^{-2.76}$, incorporating trigonal warping, finite F, and k-dependent spin-orbit interaction, with $G \neq 0$. The black squares are the nonlinear transport measurements data of Ref. [24] at $T = 100$ mK. Inset: representation of the $\varepsilon_{\pm}(\mathbf{k})$ bands featuring a Weyl node at the origin in $\mathbf{k}$-space.

that this requirement is indeed satisfied. The results are presented in Fig. 3. Our results show that the polarization is indeed mostly oriented along the x axis, $\mathbf{P}\| \pm \hat{\mathbf{x}}$, with a magnitude of roughly $\pm 18 \mu C/cm^2$ at zero applied electric field, for α-Te (+) and α'-Te (−) [38,42], and is robust under variations of an external field applied along the x axis. We have also observed a small polarization component perpendicular to the film, $\mathbf{P}\| \mp \hat{\mathbf{y}}$, while the component along the coil direction was always zero, a consequence of the lone pair geometry.

Discussion—We now compare our results to second harmonic transport experiments on 2D α-Te that have been previously reported in Ref. [24] using the setup shown in Fig. 1(a). Phase sensitive measurements with magnetic fields up to 10T revealed the antisymmetric resistance $\Delta R \equiv R(B, I) - R(B, -I)$ between opposite current directions [24]. A driving ac current in the small frequency, dc limit, of $I = 12$ μA was injected into the system and both the longitudinal voltage, V^{ω}_{zz}, and its second harmonic, $V^{2\omega}_{zz}$, were measured. The resulting unidirectional magnetoresistance was found to be linear in both $\mathbf{B}$ and $\mathbf{I}$, as reported in [24]. The proportionality coefficient $\gamma^{\pm}$ is chirality sensitive and, combined with the net polarization $\mathbf{P}$, produces the phenomenology described by Eq. (4). For magnetic field rotations in the $y-z$ (θ rotation) and $x-y$ (ϕ rotation) planes, the angular dependence of the eMChA coefficient follows $\cos\theta$ and $\cos\phi$ functions, respectively [24,29]. This behavior is consistent with Eq. (4) for the dominant polarization component, $\mathbf{P}\|\mathbf{x}$ [Figs. 4(a) and 4(b)], and provides further evidence for the polar nature of the eMChA effect in tellurene. Importantly, a smaller, nonzero, and so far undetected, $\mathbf{P}$ component perpendicular to the film, $\mathbf{P}\| - \mathbf{y}$, explains the much smaller eMChA coefficient ($\sim 10^{-6}$ T^{-1}) observed for rotations in the z-x plane (α rotation) [29], which follows a $-\sin\alpha$ function [Fig. 4(c)]. This constitutes a truly remarkable finding (not sample misalignment, see [29]) and a final piece of evidence toward a polar nature for the eMChA in tellurene.

To test the universal scaling predicted in Eq. (15), a gate voltage was used to control the carrier population in the conduction band [24], through $n(V) = \kappa V$ [29]. Because in 2D $\mu(V) = V\pi\hbar^2\kappa/(m^*_+ + m^*_-)$ [29] and since $\sigma(V) = n(V)e^2\tau/m^*$, we find that the normalized $\gamma^{\pm}(\mu)$ coefficient in Eq. (4) decreases following $\gamma^{\pm}(V) \sim G(V)/\sigma(V) \sim V^{-5/2}$, as shown in Fig. 4(d). This is a genuine quantum geometric effect and results from the Fermi surface moving away from the Weyl node and toward regions in the Hilbert space of increasingly Euclidean character, as shown in Fig. 1(b).

Conclusions—We have shown that the eMChA in noncentrosymmetric polar media owes its existence to the quantum geometric properties and to large Born effective charges. We have laid Rikken's conjecture on solid theoretical ground, and we unveiled a scaling relationship between the eMChA coefficient and the chemical potential, $\gamma^{\pm}(\mu) \sim \mu^{-5/2}$ [29], which we verified experimentally by comparison to available phase sensitive transport measurements in 2D Te under applied gate voltage, V [24]. Remarkably, we have shown that the voltage, V, can be used to fine-tune the position of the chemical potential, μ, relative to the Weyl node, where the eMChA becomes maximized, providing a novel mechanism for quantum geometric rectification [see inset of Fig. 4(d)]. Our work further demonstrates the full control of rectification by varying $\mathbf{I}$, $\mathbf{P}$, $\mathbf{B}$, and V, opening up new venues for the understanding of nonreciprocal phenomena in advanced quantum materials and paving the way for the design, production, and control of rectification devices [14].

Acknowledgments—P. F. acknowledges support of the program Investigo (Reference No. 200076ID6/BDNS 664047) funded by the European Union through the Recovery, Transformation and Resilience Plan NextGenerationEU. V. V. acknowledges financial support from PNRR MUR (Project No. PE0000023-NQSTI) and PRIN 2022 (Protocol No. 20228YCYY7). This work is

supported by the Brazilian funding agencies FAPERJ and CNPq.

Data availability—The data that support the findings of this Letter are openly available [1].

[1] C. Alexander and M. Sadiku, *Fundamentals of Electric Cirtuits* (McGraw-Hill Education, New York, 2016).

[2] R. W. Erickson and D. Maksimović, *Fundamentals of Power Electronics* (Springer, Cham, Switzerland, 2020).

[3] Y. Tokura and N. Nagaosa, Nonreciprocal responses from non-centrosymmetric quantum materials, Nat. Commun. **1**, 3740 (2018).

[4] J. Wade, J. N. Hilfiker, J. R. Brandt, L. Liirò-Peluso, L. Wan, X. Shi, F. Salerno, S. T. J. Ryan, S. Schöche, O. Arteaga, T. Jávorfi, G. Siligardi, C. Wang, D. B. Amabilino, P. H. Beton, A. J. Campbell, and M. J. Fuchter, Natural optical activity as the origin of the large chiroptical properties in $\pi-$conjugated polymer thin films, Nat. Commun. **11**, 6137 (2020).

[5] L. Wang, L. Shen, H. Bai, H.-A. Zhou, K. Shen, and W. Jiang, Electrical excitation and detection of chiral magnons in a compensated ferrimagnetic insulator, Phys. Rev. Lett. **133**, 166705 (2024).

[6] T. Kahana, D. A. B. Lopez, and D. M. Juraschek, Light-induced magnetization from magnonic rectification, Sci. Adv. **10**, eado0722 (2024).

[7] Y. Li, Y. Li, P. Li, B. Fang, X. Yang, Y. Wen, D. Zheng, C. Zhang, X. He, A. Manchon, Z.-H. Cheng, and X. Zhang, Nonreciprocal charge transport up to room temperature in bulk Rashba semiconductor $\alpha-$GeTe, Nat. Commun. **12**, 540 (2021).

[8] G. L. J. A. Rikken and P. Wyder, Magnetoelectric anisotropy in diffusive transport, Phys. Rev. Lett. **94**, 016601 (2005).

[9] T. Ideue, K. Hamamoto, S. Koshikawa, M. Ezawa, S. Shimizu, Y. Kaneko, Y. Tokura, N. Nagaosa, and Y. Iwasa, Bulk rectification effect in a polar semiconductor, Nat. Phys. **6**, 578 (2017).

[10] R. Yoshimi, M. Kawamura, K. Yasuda, A. Tsukazaki, K. S. Takahashi, M. Kawasaki, and Y. Tokura, Nonreciprocal electrical transport in the multiferroic semiconductor (Ge, Mn)Te, Phys. Rev. B **106**, 115202 (2022).

[11] H. F. Legg, M. Rößler, F. Münning, D. Fan, O. Breunig, A. Bliesener, G. Lippertz, A. Uday, A. A. Taskin, D. Loss, J. Klinovaja, and Y. Ando, Giant magnetochiral anisotropy from quantum-confined surface states of topological insulator nanowires, Nat. Nanotechnol. **7**, 696 (2022).

[12] Y. Liu, T. Holder, and B. Yan, Chirality-induced giant unidirectional magnetoresistance in twisted bilayer graphene, Innovation **2**, 100085 (2021).

[13] Y. Wang, H. F. Legg, T. Bömerich, J. Park, S. Biesenkamp, A. A. Taskin, M. Braden, A. Rosch, and Y. Ando, Gigantic magnetochiral anisotropy in the topological semimetal $ZrTe_5$, Phys. Rev. Lett. **128**, 176602 (2022).

[14] R. Dalven, *Introduction to Applied Solid State Physics* (Springer, New York, 1990).

[15] G. L. J. A. Rikken, C. Strohm, and P. Wyder, Observation of magnetoelectric directional anisotropy, Phys. Rev. Lett. **89**, 133005 (2002).

[16] J. D. Jackson, *Classical Electrodynamics* 3rd ed. (Wiley, New York, 1999).

[17] P. Hertel, *Lectures on Theoretical Physics Linear Response Theory* (University of Osnabrück, Osnabrück, 2005).

[18] T. Liu, X.-B. Qiang, H.-Z. Lu, and X. C. Xie, Quantum geometry in condensed matter, Natl. Sci. Rev. **12**, nwae334 (2025).

[19] J. M. Ziman, *Principles of the Theory of Solids* 2nd ed. (Cambridge University Press, Cambridge, England, 1972).

[20] D. Kaplan, T. Holder, and B. Yan, Unification of nonlinear anomalous hall effect and nonreciprocal magnetoresistance in metals by the quantum geometry, Phys. Rev. Lett. **132**, 026301 (2024).

[21] N. Wang, D. Kaplan, Z. Zhang, T. Holder, N. Cao, A. Wang, X. Zhou, F. Zhou, Z. Jiang, C. Zhang, S. Ru, H. Cai, K. Watanabe, T. Taniguchi, B. Yan, and W. Gao, Quantum-metric-induced nonlinear transport in a topological antiferromagnet, Nature (London) **621**, 487 (2023).

[22] T. Holder, D. Kaplan, and B. Yan, Consequences of time-reversal-symmetry breaking in the light-matter interaction: Berry curvature, quantum metric, and diabatic motion, Phys. Rev. Res. **2**, 033100 (2020).

[23] T. B. Smith, L. Pullasseri, and A. Srivastava, Momentum-space gravity from the quantum geometry and entropy of Bloch electrons, Phys. Rev. Res. **4**, 013217 (2022).

[24] C. Niu, G. Qiu, Y. Wang, P. Tan, M. Wang, J. Jian, H. Wang, W. Wu, and P. D. Ye, Tunable chirality-dependent nonlinear electrical responses in 2D tellurium, Nano Lett. **23**, 8445 (2023).

[25] Y. Jiang, Q. Yi, and B. Yan, Electrical magnetochiral anisotropy and quantum metric in chiral conductors, 2D Mater. **12**, 015020 (2024).

[26] G. Qiu, A. Charnas, C. Niu, Y. Wang, W. Wu, and P. D. Ye, The resurrection of tellurium as an elemental two-dimensional semiconductor, npj 2D Mater. Appl. **6**, 17 (2022).

[27] G. L. J. A. Rikken and N. Avarvari, Strong electrical magnetochiral anisotropy in tellurium, Phys. Rev. B **99**, 245153 (2019).

[28] L. E. Golub, E. L. Ivchenko, and B. Spivak, Electrical magnetochiral current in tellurium, Phys. Rev. B **108**, 245202 (2023).

[29] See Supplemental Material at http://link.aps.org/supplemental/10.1103/7nxc-j62y for further details regarding the $\mathbf{k}\cdot\mathbf{p}$ perturbation theory, corrections to the Boltzmann equation arising from topological terms, the geodesic contribution to the velocity, an additional description of the experimental setup, and the DFT calculations, which includes Ref. [30].

[30] T. Sohier, M. Calandra, and F. Mauri, Density functional perturbation theory for gated two-dimensional heterostructures: Theoretical developments and application to flexural phonons in graphene, Phys. Rev. B **96**, 075448 (2017).

[31] J. Cayssol and J. N. Fuchs, Topological and geometrical aspects of band theory, J. Nonlinear Opt. Phys. Mater. **4**, 034007 (2021).

[32] D. Xiao, M.-C. Chang, and Q. Niu, Berry phase effects on electronic properties, Rev. Mod. Phys. **82**, 1959 (2010).

[33] G. P. Maruggi, J. Ferreira, E. Baggio-Saitovitch, C. Enderlein, and M. B. Silva Neto, Hedgehog orbital texture

in p-type tellurium and the antisymmetric nonreciprocal hall response, Phys. Rev. Mater. **7**, 014204 (2023).
[34] M. Kang, S. Kim, Y. Qian, P. M. Neves, L. Ye, J. Jung, D. Puntel, F. Mazzola, S. Fang, C. Jozwiak, A. Bostwick, E. Rotenberg, J. Fuji, I. Vobornik, J.-H. Park, J. Checkelsky, B.-J. Yang, and R. Comin, Measurements of the quantum geometric tensor in solids, Nat. Phys. **21**, 110 (2025).
[35] A. Lavasani, D. Bulmash, and S. Das Sarma, Wiedemann-franz law and fermi liquids, Phys. Rev. B **99**, 085104 (2019).
[36] F. Rittweger, N. F. Hinsche, and I. Mertig, Phonon limited electronic transport in pb, J. Phys. Condens. Matter **29**, 355501 (2017).
[37] A. M. Ganose, J. Park, A. Faghaninia, R. Woods-Robinson, K. A. Persson, and A. Jain, Efficient calculation of carrier scattering rates from first principles, Nat. Commun. **12**, 2222 (2021).
[38] J. Zhang, J. Zhang, Y. Qi, S. Gong, H. Xu, Z. Liu, R. Zhang, M. Sadi, D. Sychev, R. Zhao, H. Yang, Z. Wu, D. Cui, L. Wang, C.-L. Ma, X. Wu, J. Gao, Y. Chen, X. Wang, and Y. Jiang, Room-temperature ferroelectric, piezoelectric and resistive switching behaviors of single-element te nanowires, Nat. Commun. **15**, 7648 (2024).
[39] J. Blinowski, G. Rebmann, C. Rigaux, and J. Mycielski, Magnetooptical investigation of the conduction band in tellurium, J. Phys. II (France) **38**, 1139 (1977).
[40] P. Giannozzi *et al.*, Quantum espresso: A modular and open-source software project for quantum simulations of materials, J. Phys. Condens. Matter **21**, 395502 (2009).
[41] J. M. Soler, E. Artacho, J. D. Gale, A. García, J. Junquera, P. Ordejón, and D. Sánchez-Portal, The SIESTA method for *ab initio* order-N materials simulation, J. Phys. Condens. Matter **14**, 2745 (2002).
[42] Z.-H. Zhang, L.-Z. Yang, H.-J. Qin, W.-A. Liao, H. Liu, J. Fu, H. Zeng, W. Zhang, and Y.-S. Fu, Direct observations of spontaneous in-plane electronic polarization in 2D Te films, Adv. Mater. **36**, 2405590 (2024).